1   **Downscaling Surface Wind Predictions from Numerical Weather Prediction Models in**

2   **Complex Terrain with WindNinja**

3

4   **N.S. Wagenbrenner[1], J.M. Forthofer[1], B.K. Lamb[2], K.S. Shannon[1], B.W. Butler[1]**

5   [1]{US Forest Service, Rocky Mountain Research Station, Missoula Fire Sciences Laboratory,
6   5775 W Highway 10, Missoula, MT 59808, USA}

7   [2]{Laboratory for Atmospheric Research, Department of Civil and Environmental Engineering,
8   Washington State University, Pullman, WA 99164, USA}

9   Correspondence to: N.S. Wagenbrenner (nwagenbrenner@fs.fed.us)

10

11

12   **Abstract**

13   Wind predictions in complex terrain are important for a number of applications. Dynamic

14   downscaling of numerical weather prediction (NWP) model winds with a high resolution wind

15   model is one way to obtain a wind forecast that accounts for local terrain effects, such as wind

16   speed-up over ridges, flow channeling in valleys, flow separation around terrain obstacles, and

17   flows induced by local surface heating and cooling. In this paper we investigate the ability of a

18   mass-consistent wind model for downscaling near-surface wind predictions from four NWP

19   models in complex terrain. Model predictions are compared with surface observations from a

20   tall, isolated mountain. Downscaling improved near-surface wind forecasts under high-wind

21   (near-neutral atmospheric stability) conditions. Results were mixed during upslope and

22   downslope (non-neutral atmospheric stability) flow periods, although wind direction

23   predictions generally improved with downscaling. This work constitutes evaluation of a

24   diagnostic wind model at unprecedented high spatial resolution in terrain with topographical

25   ruggedness approaching that of typical landscapes in the western US susceptible to wildland

26   fire.

27

28

1. Introduction

29

30 Researchers from multiple disciplines rely on routine forecasts from numerical weather

31 prediction (NWP) models to drive transport and dispersion models, conduct wind assessments

32 for wind energy projects, and predict the spread of wildfires. These applications require fine-

33 scale, near-surface wind predictions in regions where rugged terrain and vegetation have a

34 significant effect on the local flow field. Terrain effects such as wind speed-up over ridges, flow

35 channeling in valleys, flow separation around terrain obstacles, and enhanced surface

36 roughness alter the flow field over spatial scales finer than those used for routine, operational

37 NWP forecasting.

38

39 Numerous operational mesoscale NWP model forecast products are available in real-time, such

40 as those provided by National Centers for Environmental Prediction (NCEP). Access to these

41 output products is facilitated by automated archiving and distribution systems such as the

42 National Operational Model Archive and Distribution System (NOMADS). These routine

43 forecast products are highly valuable to researchers and forecasters, for example, as inputs to

44 drive other models. In many cases, however, the spatial resolution of the system of interest

45 (e.g., wildland fire spread) is much finer than that of the NWP model output.

46

47 The model grid horizontal resolution in operational NWP models is limited due, in part, to the

48 high computational demands of NWP. Routine gridded forecast products are typically provided

49 at grid resolutions of 3 km or larger. The High Resolution Rapid Refresh (HRRR) model produces

50 3-km output grids and is currently the highest-resolution operational forecast in the U.S.

51

52   NWP models have been run successfully with grid resolutions of less than 1 km in complex

53   terrain for specific cases when modifications were made to the meshing (Lundquist et al. 2010)

54   or PBL schemes (Ching et al., 2014; Seaman et al., 2012) or when large-eddy simulation (LES)

55   was used (Chow and Street, 2008). While successful for specific test cases, these efforts

56   employ specialized model configurations that have not been incorporated into routine

57   forecasting frameworks, either because they are not sufficiently robust, have not been

58   thoroughly tested, or are too computationally intense for routine forecasting. For example, the

59   configuration used in Seaman et al. (2012) is applicable for stable nocturnal conditions only.

60

61   Additionally, these modifications require technical expertise in NWP and access to substantial

62   computing resources, which many consumers of NWP output do not have. Perhaps, the biggest

63   limitation to running NWP models on grids with fine horizontal resolution is the computational

64   demand. Time-sensitive applications, such as operational wildland fire support, require fast

65   solution times (e.g., less than 1 hr) on simple hardware (e.g., laptop computers with 1-2

66   processors). Thus, there remains a practical need for fast-running tools that can be used to

67   downscale coarse NWP model winds in complex terrain.

68

69   Dynamic downscaling with a steady-state (diagnostic) wind model is one option for obtaining

70   near-surface high-resolution winds from routine NWP model output (e.g., Beaucage et al.,

71   2014). The NWP model provides an initial wind field that accounts for mesoscale dynamics

72   which is then downscaled by a higher resolution wind model to enforce conservation of mass

73   and, in some cases, momentum and energy on the flow field on a higher resolution grid that

74   better resolves individual terrain features. Dynamic downscaling can be done in a steady-state

75   fashion for each time step of the NWP model output. One advantage of using a steady-state

76   downscaling approach is that the spatial resolution can be increased with no additional

77   computational cost associated with an increase in temporal resolution.

78

79   Diagnostic wind models have primarily been evaluated with observations collected over

80   relatively simple, low elevation hills. Askervein Hill (Taylor and Teunissen, 1987) and Bolund Hill

81   (Berg et al., 2011) are the two mostly commonly used datasets for evaluating diagnostic wind

82   models. These are both geometrically simple, low-elevation hills compared to the complex

83   terrain exhibited in many regions of the western U.S. susceptible to wildland fire. Lack of

84   evaluations under more complex terrain is due in part to the lack of high-resolution datasets

85   available in complex terrain. Recently, Butler et al. (2015) reported high-resolution wind

86   observations from a tall, isolated mountain (Big Southern Butte) in the western U.S. Big

87   Southern Butte is substantially taller and more geometrically complex than both Askervein and

88   Bolund hills.

89

90   In this work, we investigate the ability of a mass-conserving wind model, WindNinja (Forthofer

91   et al., 2014a), for dynamically downscaling NWP model winds over Big Southern Butte.

92   WindNinja is a diagnostic wind model developed for operational wildland fire support. It is

93   primarily designed to simulated mechanical effects of terrain on the flow, which are most

94   important under high-wind conditions; however, WindNinja also contains parameterizations for

95   local thermal effects, which are more important under periods of weak external forcing.

96   WindNinja has primarily been evaluated under high-wind conditions, which are thought to be

97   most important for wildland fire behavior, and so these the thermal parameterizations have not

98   been thoroughly tested. WindNinja has previously been evaluated against the Askervein Hill

99   data (Forthofer et al., 2014a) and found to capture important terrain-induced flow features,

100   such as ridgetop speed-up, and it has been shown to improve wildfire spread predictions in

101   complex terrain (Forthofer et al., 2014b). We focus on downscaling wind in this work because it

102   is typically more spatially and temporally variable than temperature or relative humidity, and

103   thus, more important to predict at high spatial resolution. Wind is also often the driving

104   environmental variable for wildfire behavior.

105

106   The goals of this work were to (1) investigate the accuracy of NWP model near-surface wind

107   predictions in complex terrain on spatial scales relevant for processes driven by local surface

108   winds, such as wildland fire behavior and (2) assess the ability of a mass-consistent wind model

109   to improve these predictions through dynamic downscaling. Wind predictions are investigated

110   from four NWP models operated on different horizontal grid resolutions. This work constitutes

111   one of the first evaluations of a diagnostic wind model with data collected over terrain with a

112   topographical ruggedness approaching that of western U.S. landscapes susceptible to wildland

113   fire.

114

115   **2. Model descriptions and configurations**

116   WRF is a NWP model that solves the non-hydrostatic, fully compressible Navier-Stokes

117   equations using finite difference method (FDM) discretization techniques (Skamarock et al.,

118   2008). All of the NWP models investigated in this work use either the Advanced Research WRF

119   (ARW) or the non-hydrostatic multi-scale model (NMM) core of the WRF model (Table 1).

120   *2.1. Routine Weather Research and Forecasting (WRF-UW)*

121   Routine WRF-ARW forecasts with 4 km horizontal grid resolution were acquired from the

122   University of Washington Atmospheric Sciences forecast system

123   (www.atmos.washington.edu/mm5rt/info.html). These forecasts are referred to as WRF-UW.

124   The outer domain of WRF-UW has a horizontal grid resolution of 36 km and covers most of the

125   western US and northeastern Pacific Ocean. This outer domain is initialized with NCEP Global

126   Forecast System (GFS) 1-degree runs. The 36 km grid is nested down to 12 km, 4 km, and an

127   experimental 1.33 km grid which covers a limited portion of the Pacific Northwest. The 4 km

128   grid investigated in this study covers the Pacific Northwest, including Washington, Oregon,

129   Idaho, and portions of California, Nevada, Utah, Wyoming, and Montana. Physical

130   parameterizations employed by WRF-UW include the Noah Land Surface Model (Chen et al.,

131   1996), Thompson microphysics (Thompson et al., 2004), Kain-Fritsch convective scheme (Kain,

132   2004), Rapid Radiative Transfer Model (RRTM) for longwave radiation (Mlawer et al., 1997),

133   Duhdia (1989) for shortwave radiation, and the Yonsei University (YSU) boundary layer scheme

134   (Hong et al., 2006). WRF-UW is run at 00z and 12z and generates hourly forecasts out to 84

135   hours. The computational domain consists of 38 vertical layers. The first grid layer is

136   approximately 40 m AGL and the average model top height is approximately 16000 m AGL.

137 *2.2. Weather Research and Forecasting Reanalysis (WRF-NARR)*

138 WRF-ARW reanalysis runs were performed using the NCEP North American Regional Reanalysis

139 (NARR) data (Mesinger et al., 2006). The reanalysis runs are referred to as WRF-NARR. The

140 same parameterizations and grid nesting structures used in WRF-UW were also used for the

141 WRF-NARR simulations, except that the WRF-NARR inner domain had 33 vertical layers and a

142 horizontal grid resolution of 1.33 km (Table 1). Analysis nudging (e.g., Stauffer and Seaman,

143 1994) was used above the boundary layer in the outer domain (36 km horizontal grid

144 resolution). Hourly WRF-NARR simulations were run for 15 day periods with 12 hours of model

145 spin up prior to each simulation. The first grid layer was approximately 38 m AGL and the

146 average model top height was approximately 15000 m AGL. WRF-NARR differs from the other

147 models used in this study in that it is not a routinely run model. These were custom simulations

148 conducted by our group to provide a best-case scenario for the NWP models. Routine forecasts

149 are already available for limited domains (e.g., UW provides WRF simulations on a 1.33 km grid

150 for a small domain in the Pacific Northwest of the US) and are likely to become more widely

151 available at this grid resolution in the near future.

152 *2.3. North American Mesoscale Model (NAM)*

153 The North American Mesoscale (NAM) model is an operational forecast model run by NCEP for

154 North America (http://www.emc.ncep.noaa.gov/index.php?branch=NAM). The NAM model

155 uses the NMM core of the WRF model. The NAM CONUS domain investigated in this study has

156 a horizontal grid resolution of 12 km. NAM employs the Noah Land Surface model (Chen et al.,

157 1996), Ferrier et al. (2003) for microphysics, Kain (2004) for convection, GFDL (Lacis and

158   Hansen, 1974) for longwave and shortwave radiation, and the Mellor-Yamada-Janjic (MJF)

159   boundary layer scheme (Janjic, 2002). The NAM model is initialized with 12-hr runs of the NAM

160   Data Assimilation System. It is run four times daily at 00z, 06z, 12z, and 18z and generates

161   hourly forecasts out to 84 hours. The computational domain consists of 26 vertical layers. The

162   first grid layer is approximately 200 m AGL and the average model top height is approximately

163   15000 m AGL. NAM forecasts are publicly available in real time from NCEP. Although the 12-

164   km horizontal resolution used in NAM is not sufficient to resolve the butte, this resolution is

165   sufficient for resolving the surrounding Snake River Plain and therefore can be used to generate

166   a domain-average flow for input to WindNinja.

167   *2.4. High Resolution Rapid Refresh (HRRR)*

168   The High Resolution Rapid Refresh (HRRR) system is a nest inside of the NCEP-Rapid Refresh

169   (RAP) model (13 km horizontal grid resolution; http://ruc.noaa.gov/hrrr/). HRRR has a

170   horizontal grid resolution of 3 km and is updated hourly. HRRR uses the WRF model with the

171   ARW core and employs the RUC-Smirnova Land Surface Model (Smirnova et al., 1997; Smirnova

172   et al., 2000), Thompson et al. (2004) microphysics, RRTM longwave radiation (Mlawer et al.,

173   1997), Goddard shortwave radiation (Chou and Suarez, 1994), the MYJ boundary layer scheme

174   (Janjic, 2002). HRRR is initialized from 3-km grids with 3-km radar assimilation over a 1-hr

175   period. HRRR is currently the highest resolution operational forecast available in real time. The

176   computational domain consists of 51 vertical layers. The first grid layer is approximately 8 m

177   AGL and the average model top height is approximately 16000 m AGL.

178   *2.5. WindNinja*

179 WindNinja is a mass-conserving diagnostic wind model developed and maintained by the USFS

180 Missoula Fire Sciences Laboratory (Forthofer et al., 2014a). The theoretical formulation is

181 described in detail in Forthofer et al. (2014a). Here we provide a brief overview of the

182 modeling framework. WindNinja uses a variational calculus technique to minimize the change

183 in an initial wind field while conserving mass locally (within each cell) and globally over the

184 computational domain. The numerical solution is obtained using finite element method (FEM)

185 techniques on a terrain-following mesh consisting of layers of hexahedral cells that grow

186 vertically with height.

187

188 WindNinja includes a diurnal slope flow parameterization (Forthofer et al., 2009). The diurnal

189 slope flow model used in WindNinja is the shooting flow model in Mahrt (1982). It is a one-

190 dimensional model of buoyancy-driven flow along a slope. A micrometeorological model

191 similar to the one used in CALMET (Scire et al., 2000; Scire and Robe, 1997) is used to compute

192 surface heat flux, Monin-Obukhov length, and boundary layer height. The slope flow is then

193 calculated as a function of sensible heat flux, distance to ridgetop or valley bottom, slope

194 steepness, and surface and entrainment drag parameters. The slope flow is computed for each

195 grid cell and added to the initial wind in that grid cell. Additional details can be found in

196 Forthofer et al. (2009).

197

198 WindNinja was used to dynamically downscale hourly 10-m wind predictions from the above

199 NWP models. The WindNinja computational domain was constructed from 30-m resolution

200   Shuttle Radar Topography Mission (SRTM) data (Farr et al., 2007). The 10-m NWP winds were

201   bilinearly interpolated to the WindNinja computational domain and used as the initial wind

202   field. Layers above and below the 10-m height were fit to a logarithmic profile (neutral

203   atmospheric stability) based on the micrometeorological model. The computational domain

204   consisted of 20 vertical layers. The first grid layer is 1.92 m AGL and the average model top

205   height is 931 m AGL.

206   *2.6. Terrain representation*

207   The four NWP models used in this study employ an implementation of the WRF model. They

208   use different initial and boundary conditions, incorporate different parameterizations for sub-

209   grid processes, such as land surface fluxes, convection, and PBL evolution, but in terms of

210   surface wind predictions under the conditions investigated in this study (inland, dry

211   summertime conditions), the horizontal grid resolution is arguably the most important

212   difference among the models. The horizontal grid resolution affects the numerical solution

213   since fewer terrain features are resolved by coarser grids. Coarser grids essentially impart a

214   smoothing effect which distorts the actual geometry of the underlying terrain (Fig. 1). As

215   horizontal cell size and terrain complexity increase, the accuracy of the terrain representation

216   and thus, the accuracy of the near-surface flow solution deteriorate.

217
218   **3. Evaluations with field observations**

219   *3.1. Observations at Big Southern Butte*

11

220   Surface wind data (Butler et al., 2015) collected from an isolated mountain (Big Southern Butte,

221   hereafter 'BSB'; 43.395958, -113.02257) in southeast Idaho were used to evaluate surface wind

222   predictions (Fig. 1). BSB is a predominantly grass-covered volcanic cinder cone with a

223   horizontal scale of 5 km and a vertical scale of 800 m and surrounded in all directions by the

224   relatively flat Snake River Plain. The portion of the Snake River Plain surrounding BSB slopes

225   downward gently from the northeast to the southwest.

226

227   Three-meter wind speeds and directions were measured with cup-and-vane anemometers at

228   53 locations on and around BSB. The anemometers have a measurement range of 0 to 44 m s^{-1},

229   a resolution of 0.19 m s^{-1} and 1.4°, and are accurate to within ±0.5 m s^{-1} and ±5°. The

230   anemometers measured wind speed and direction every second and logged 30-s averages. We

231   averaged these 30-s winds over a 10-min period at the top of each hour (five minutes before

232   and 5 minutes after the hour). The 10-min averaging period was chosen to correspond roughly

233   with the time scale of wind predictions from the NWP forecasts. The NWP output is valid at a

234   particular instant in time, but there is always some inherent temporal averaging in the

235   predictions. The temporal averaging associated with a given prediction depends on the time-

236   step used in the NWP model and is typically on the order of minutes. The 10-min averaged

237   observed data are referred to in the text as 'hourly' observations (since they are averaged at

238   the top of each hour) and are compared directly with the hourly model predictions.

239

240   Butler et al. (2015) observed the following general flow features at BSB. During periods of weak

241   synoptic and mesoscale forcing (hereafter, referred to collectively as 'external forcing'), the

242   observed surface winds at BSB were decoupled from the large-scale atmospheric flows, except

243   for at high-elevation ridgetop locations. Diurnal slope flows dominated the local surface winds

244   under periods of weak external forcing. There were frequent periods of strong external forcing,

245   during which the diurnal slope winds on BSB were completely overtaken by the larger-scale

246   winds. These periods of strong external forcing at BSB were typically characterized by large-

247   scale southwesterly flow aligned with the Snake River Plain, although occasionally there were

248   also strong early morning winds from the northeast. Under periods of strong external forcing

249   wind speeds commonly varied by as much as 15 m s^{-1} across the domain due to mechanical

250   effects of the terrain (e.g., speed-up over ridges and lower speeds on leeward slopes).

251   Additional details regarding the BSB field campaign can be found in Butler et al. (2015).

252   *3.2. Evaluation methods*

253   Hourly observations were compared against corresponding hourly predictions from the most

254   recent model run. Modeled and observed winds were compared by interpolating the modeled

255   surface wind variables to the observed surface sensor locations at each site. The 10-m winds

256   from the NWP forecasts were interpolated to sensor locations, using bilinear interpolation in

257   the horizontal dimension and a log profile in the vertical dimension. A 3-D interpolation

258   scheme was used to interpolate WindNinja winds to the sensor locations. This 3-D

259   interpolation was possible because the WindNinja domain had layers above and below the

260   surface sensor height (3.0 m AGL). A 3-D interpolation scheme was not possible for the NWP

261   domains since there were not any layers below the three meter surface sensor height.

262

263   Model performance was quantified in terms of the mean bias, root-mean-square error (RMSE),

264   and standard deviation of the error (SDE):

265    $$\overline{\varphi'} = \frac{1}{N}\sum_{i=1}^{N}\varphi'$$ (1)

266    $$\text{RMSE} = \left[\frac{1}{N}\sum_{i=1}^{N}(\varphi'_i)^2\right]^{1/2}$$ (2)

267    $$\text{SDE} = \left[\frac{1}{N-1}\sum_{i=1}^{N}(\varphi'_i - \overline{\varphi'})^2\right]^{1/2}$$ (3)

268   where φ' is the difference between simulated and observed variables and N is the number of

269   observations.

270   *3.3. Case selection*

271   We selected a five-day period from July 15-19 2010 for model evaluations. This specific period

272   was chosen because it included periods of both strong and weak external forcing, conditions

273   were consistently dry and sunny, and was a period for which we were able to acquire forecasts

274   from all NWP models selected for investigation in this study.

275

276   The observed data from the five-day period were broken into periods of upslope, downslope,

277   and externally-driven flow conditions to further investigate model performance under these

278   particular types of flow regimes. We used the partitioning schemes described in Butler et al.

279   (2015). Externally-driven events were partitioned out by screening for hours during which wind

280   speeds at a designated sensor (R2, located 5 km southwest of the butte in flat terrain) exceeded

281   a predetermined threshold wind speed of 6 m s^{-1}. This sensor was chosen because it was

282   located in flat terrain far from the butte and therefore was representative of near-surface

283   winds that were largely unaffected by the butte itself. Hours of upslope and downslope flows

284   (i.e., observations under weak external forcing) were then partitioned out of the remaining

285   data. Additional details regarding the partitioning scheme can be found in Butler et al. (2015).

286   Statistical metrics were computed for these five-day periods.

287   We also chose one specific hour representative of each flow regime within the 5-day period to

288   qualitatively investigate model performance for single flow events under the three flow

289   regimes. This directly comparison of NWP model predictions, downscaled predictions, and

290   observations for single events in order to get a visual sense for how the models performed

291   spatially while avoiding any inadvertent complicating issues that may have arose from temporal

292   averaging over the flow regimes.

293   **4. Results and discussion**

294   *4.1. Overview of the five-day simulations*

295   Fig. 2 shows observed vs. forecasted wind speeds during the five-day period. The following

296   generalizations can be made. The NWP models predicted wind speeds below 5 m s^{-1}

297 reasonably well on average, although HRRR tended to over predict at speeds below 3 m s^{-1} (Fig.

298 2). There is a lot of scatter about the regression lines, but the regressions follow the line of

299 agreement fairly well up to observed speeds around 5 m s^{-1}. Downscaling did not improve wind

300 speed predictions much in this range. NWP forecast accuracy declined for observed speeds

301 between 5 and 10 m s^{-1}, and accuracy sharply dropped off for observed speeds above 10 m s^{-1}.

302 This is indicated by the rapid departure of the NWP model regression lines from the line of

303 agreement (Fig 2). Downscaling improved wind speed predictions for all NWP forecasts for

304 observed speeds greater than around 5 m s^{-1} and the biggest improvements were for observed

305 speeds greater than 10 m s^{-1} (Fig. 2). This is indicated by the relative proximity of the

306 downscaled regression lines to the line of agreement (Fig. 2).

307

308 Poor model accuracy at higher speeds is largely due to the models under predicting windward

309 slope and ridgetop wind speeds. Observed speeds at these locations were often three or four

310 times higher than speeds in other locations in the study area (e.g., note the spatial variability in

311 Fig 3). Butler et al. (2015) showed that the highest observed speeds occurred on upper

312 elevation windward slopes and ridgetops and the lowest observed speeds occurred on the

313 leeward side of the butte and in sheltered side drainages on the butte itself. Downscaling with

314 WindNinja offers improved predictions at these locations as indicated by Fig. 2 (regression lines

315 in closer proximity to the line of agreement) and Fig. 3 (spatial variability in predictions more

316 closely matches that of the observations).

317

318   Additionally, the downscaled NAM wind speeds were as accurate as the downscaled HRRR and

319   WRF-UW wind speeds (Fig. 2). This indicates that the NAM forecast was able to capture the

320   important large-scale flow features around BSB such that the additional resolution provided by

321   HRRR and WRF-UW was not essential to resolve additional flow features in the large scale flow

322   around BSB.

323

324   The accuracy of the NAM forecast at BSB is likely due to the fact that Snake River Plain which

325   surrounds BSB is relatively flat and extends more than 50 km in all directions from the butte.

326   Even a 12 km grid resolution would be capable of resolving the Snake River Plain and diurnal

327   flow patterns within this large, gentle-relief drainage. Coarse-resolution models would not be

328   expected to offer this same level of accuracy in areas of more extensive complex terrain,

329   however. In areas surrounded by highly complex terrain it may be necessary to acquire NWP

330   model output on finer grids in order to resolve the regional flow features.

331

332   The NWP forecasts predicted the overall temporal trend in wind speed (Fig. 3), but

333   underestimated peak wind speeds due to under predictions on ridgetops and windward slopes

334   as previously discussed, and also occasionally in the flat terrain on the Snake River Plain

335   surrounding the butte (Fig. 4).

336

337 NWP models with coarser resolution grids predicted less spatial variability in wind speed (Fig.

338 3). This is because there were fewer grid cells covering the domain, and thus fewer prediction

339 points around the butte. The spatial variability in the downscaled wind speed predictions more

340 closely matched that of the observed data, although the highest speeds were still under

341 predicted (Fig. 3). Although downscaling generally improved the spatial variability of the

342 predictions, there were cases where NWP errors clearly propagated into the downscaled

343 simulations. For example, HRRR frequently over predicted morning wind speeds associated

344 with down-drainage flow on the Snake River Plain; this error was amplified in the downscaled

345 simulations, especially at the ridgetop locations (e.g., Fig. 3-4, 15-17 July).

346

347 The mean bias, RMSE, and SDE for wind speed and wind direction were smaller in nearly all

348 cases for the downscaled simulations than for the NWP forecasts during the five-day period

349 (Table 2). Mean biases in wind speed were all slightly negative and NAM and WRF-UW had the

350 largest mean biases. The RMSE and SDE in wind speed were largest for HRRR. Although mean

351 bias, RMSE, and SDE in wind direction for the downscaled forecasts were smaller or equal to

352 those for the NWP forecasts, the differences were small, with a maximum reduction in mean

353 bias in wind direction of just 4°.

354

355 It is difficult to draw too many conclusions from the spatially and temporally averaged 5-day

356 statistics, however, since this period included a range of meteorological conditions (e.g., high-

357   wind events from different directions, upslope flow, downslope flow) each of which could have

358   been predicted with a different level of skill by the models. Qualitatively, however, the 5-day

359   results demonstrate that the spatial variability in the downscaled winds better matches that of

360   the observed winds at BSB (Fig. 3) and, although the reductions were small in some cases,

361   nearly all statistical metrics also improved with downscaling. The analysis is broken down by

362   flow regime in the next section for more insight into model performance.

363   *4.2. Performance under Upslope, downslope, and externally-forced flows*

364   Local solar heating and cooling was a primary driver of the flow during the slope flow regime at

365   BSB (Butler et al. 2015), with local thermal effects equal to or exceeding the local mechanical

366   effects of the terrain on the flow. Because there is weak external forcing (i.e., input wind

367   speeds to WindNinja are low), the downscaling is largely driven by the diurnal slope flow

368   parameterization in WindNinja during the slope flow regimes.

369

370   During upslope flow, the diurnal slope flow parameterization increases speeds on the windward

371   slopes and reduces speeds (or reverses flow and increases speeds, depending on the strength

372   of the slope flow relative to the prevailing flow) on lee slopes due to the opposing effects of the

373   prevailing wind and the thermal slope flow. The parameterization has the opposite effect

374   during downslope flow; windward slope speeds are reduced (or possibly increased if downslope

375   flow is strong enough to reverse the prevailing flow) and lee side speeds are enhanced.

376   *4.2.1 Wind speed*

377   The biggest improvements in wind speed predictions from downscaling occurred during

378   externally-driven flow events (Fig. 5). This is not surprising since the highest spatial variability in

379   the observed wind speeds occurred during high-wind events due to mechanically-induced

380   effects of the terrain, with higher speeds on ridges and windward slopes and lower speeds in

381   sheltered side drainages and on the lee side of the butte (Fig. 6-8). Since WindNinja is designed

382   primarily to simulate the mechanical effects of the terrain on the flow, it is during these high-

383   wind events that the downscaling has the most opportunity to improve predictions across the

384   domain. This has important implications for wildfire applications since high-wind events are

385   often associated with increased fire behavior.

386

387   The NWP models tended to under predict wind speeds on the windward slopes, ridgetops, and

388   surrounding flat terrain, and over predict on the lee side of the butte during high wind events

389   (e.g., Fig. 6). The largest NWP errors in wind speed during high wind events were on the

390   ridgetops, where speed-up occurred and the NWP under predicted speeds. These largest wind

391   speed errors were reduced by downscaling (e.g., Fig. 6). Downscaling reduced NWP wind speed

392   errors in most regions on the butte, although the general trend of under predicting wind speeds

393   on the windward side and over predicting on the lee side did not change (e.g., Fig. 6).

394

395   There were consistent improvements in predicted wind speeds from downscaling during the

396   upslope regime, although the improvements were smaller than for the externally-driven regime

397   (Fig. 5). Wind speeds were lower during the slope flow regimes than during the externally-

398   forced regime (Fig. 6-8), and thus, smaller improvements were possible with downscaling.

399   There was some speed-up predicted on the windward side of the butte during the

400   representative upslope case which appeared to match the observed wind field (Fig. 8).

401

402   Results were mixed for the downslope regime, as wind speeds improved with downscaling for

403   WRF-UW and NAM, but not for WRF-NARR or HRRR (Fig. 5). The poor wind speed predictions

404   from HRRR during the downslope regime is partly due to the fact that HRRR tended to over

405   predict early morning winds associated with down drainage flows on the Snake River Plain.

406   These errors were amplified by the downscaling, especially at ridgetop locations (Fig. 4). In

407   reality, the high-elevation ridgetop locations tended to be decoupled from lower-level surface

408   winds during the slope flow regimes due to flow stratification. WindNinja assumes neutral

409   atmospheric stability, however, so this stratification is not handled. A parameterization for

410   non-neutral atmospheric conditions is currently being tested in Windninja.

411

412   The diurnal slope flow parameterization in WindNinja resulted in lower speeds on the

413   windward side and higher speeds on the lee side of the butte for the representative downslope

414   case (Fig. 7). These downscaled speeds better matched those of the observed wind field,

415   although speeds were still under predicted for ridgetops and a few other locations around the

416   butte (Fig. 7). The high observed speeds at the ridgetop locations are not likely due to thermal

417   slope flow effects, but could be from the influence of gradient-level winds above the nocturnal

418   boundary layer. These ridgetop locations are high enough in elevation (800 m above the

419   surrounding plain) that they likely protruded out of the nocturnal boundary layer and were

420   exposed to the decoupled gradient-level winds. Butler et al. (2015) noted that ridgetop winds

421   did not exhibit a diurnal pattern and tended to be decoupled from winds at other locations on

422   and around the butte. Lack of diurnal winds at the summit of the butte is also confirmed by

423   National Oceanic and Atmospheric Administration Field Research Division (NOAA-FRD) mesonet

424   station data collected at the top of BSB (described in Butler et al., 2015;

425   http://www.noaa.inel.gov/projects/INLMet/INLMet.htm).

426

427   Under predictions on the lower slopes and on the plain surrounding the butte could be due to

428   overly weak slope flows being generated by the slope flow parameterization in WindNinja (Fig.

429   7-8). Overly weak slope flows could be caused by a number of things: improper

430   parameterization of surface or entrainment drag parameters, poor estimation of the depth of

431   the slope flow, or deficiencies in the micrometeorological model used. The slope flow

432   parameterization is being evaluated in a companion paper.

433   *4.2.2 Wind direction*

434   The biggest improvement in wind direction predictions from downscaling occurred during the

435   downslope regime (Fig. 5). Wind direction improved with downscaling for all NWP models

436   during periods of downslope flow. This indicates that the diurnal slope flow model helped to

437   orient winds downslope. This is confirmed by inspection of the vector plots for the

438   representative downslope case which show the downscaled winds oriented downslope on the

439   southwest and northeast faces of the butte (Fig. 7). Downscaling reduced speeds on the

22

440   northwest (windward) side of the butte, but did not predict strong enough downslope flow in

441   this region to reverse the flow from the prevailing northwest direction (Fig. 7). This again

442   suggests that perhaps the diurnal slope flow algorithm is predicting overly weak slope flows.

443

444   Wind direction predictions during the upslope regime also improved with downscaling for all

445   NWP models except HRRR (Fig. 5). Downscaled winds for the representative upslope case were

446   oriented upslope on the southwest (lee side) of the butte and matched the observed winds in

447   this region well (Fig. 8). This is an improvement over the NWP wind directions on the lee side of

448   the butte.

449

450   There was no improvement in wind direction predictions with downscaling during the

451   externally-driven regime (Fig. 5). Looking at the vector plots during the representative

452   externally-driven event (Fig. 6), it is clear why this would be. The representative event was a

453   high-wind event from the southwest. Wind directions are well predicted on the windward side

454   of the butte, but not on the leeward side, where the observed field indicates some recirculation

455   in the flow field (Fig. 6). The prevailing southwesterly flow is captured by the NWP model, but

456   the lee side recirculation is not. WindNinja does not predict the lee side recirculation, and thus,

457   the downscaling does not improve directions on the lee side of the butte (Fig. 7). This is an

458   expected result, as WindNinja has been shown to have difficulties simulating flows on the lee

459   side of terrain features due to the fact that it does not account for conservation of momentum

460   in the flow solution (Forthofer et al., 2014a).

5. Summary

The horizontal grid resolutions of NWP models investigated in this study were too coarse to resolve the BSB terrain. Results showed that the NWP models captured the important large-scale flow features around BSB under most conditions, but were not capable of predicting the high spatial variability (scale of 100s of meters) in the observed winds on and around the butte induced by mechanical effects of the terrain and local surface heating and cooling. Thus, surface winds from the NWP models investigated in this study would not be sufficient for forecasting wind speeds on and around the butte at the spatial scales relevant for processes driven by local surface winds, such as wildland fire spread.

Wind predictions generally improved for all NWP models by downscaling with WindNinja. The biggest improvements occurred under high-wind events (near-neutral atmospheric stability) when observed wind speeds were greater than 10 m s^{-1}. This finding has important implications for fire applications since increased wildfire behavior is often associated with high winds. Downscaled NAM wind speeds were as accurate as downscaled WRF-UW and HRRR wind speeds, indicating that a NWP model with 12 km grid resolution was sufficient for capturing the large-scale flow features around BSB.

WindNinja did not predict the observed lee-side flow recirculation at BSB that occurred during externally-forced high wind events. Previous work has shown that WindNinja has difficulties

24

481 simulating lee-side flows (Forthofer et al., 2014a). This is partly due to lack of a momentum

482 equation in the WindNinja flow solution as discussed in Forthofer et al. (2014a). Work is

483 currently underway to incorporate an optional momentum solver in WindNinja which is

484 anticipated to improve flow predictions on the lee-side of terrain obstacles.

485

486 Results indicated that WindNinja predicted overly weak slope flows compared to observations.

487 Weak slope flow could be caused by several different issues within the diurnal slope flow

488 parameterization in WindNinja: improper parameterization of surface or entrainment drag

489 parameters, poor estimation of the depth of the slope flow, or deficiencies in the

490 micrometeorological model. These issues will be explored in future work.

491

492 This work constitutes evaluation of a diagnostic wind model at unprecedented high spatial

493 resolution and terrain complexity. While extensive evaluations have been performed with data

494 collected in less rugged terrain (e.g., Askervein Hill and Bolund Hill, relatively low elevation hills

495 with simple geometry), to our knowledge, this study is the first to evaluate a diagnostic wind

496 model with data collected in terrain with topographical ruggedness approaching that of typical

497 landscapes in the western US susceptible to wildland fire. This work demonstrates that NWP

498 model wind forecasts can be improved in complex terrain, especially under high-wind events,

499 through dynamic downscaling via a mass-conserving wind model. These improvements should

500 propagate on to more realistic predictions from other model applications which are sensitive to

501   surface wind fields, such as wildland fire behavior, local-scale transport and dispersion, and

502   wind energy applications.

503   **Acknowledgements**

510

511   **References**

512   Beaucage, P., Brower, M.C., and Tensen, J.: Evaluation of four numerical wind flow models for

513   wind resource mapping, Wind Energy, 17, 197–208, 2014.

514   Berg, J., Mann, J., Bechmann, A., Courtney, M.S., and Jorgensen, H.E.: The Bolund experiment,

515   Part I: flow over a steep, three-dimensional hill, Bound.-Lay. Meteorol., 141, 219–243, 2011.

516   Butler, B.W., Wagenbrenner, N.S., Forthofer, J.M., Lamb, B.K., Shannon, K.S., Finn, D., Eckman,

517   R.M., Clawson, K., Bradshaw, L., Sopko, P., Beard, S., Jimenez, D., Wold, C., and Vosburgh,

518   M.: High-resolution observations of the near-surface wind field over an isolated mountain

519   and in a steep river canyon, Atmos. Chem. Phys., 15, 3785–3801, 2015.

520   Chen, F., Mitchell, K., Schaake, J., Xue, Y., Pan, H., Koren, V., Duan, Y., Ek, M., and Betts, A.:

521   Modeling of land-surface evaporation by four schemes and comparison with FIFE

522   observations, J. Geophys. Res., 101, 7251–7268, 1996.

523   Ching, J., Rotunno, R., LeMone, M., Martilli, A., Kosovic, B., Jimenez, P.A., and Dudhia, J.:

524   Convectively induced secondary circulations in fine-grid mesoscale numerical weather

525   prediction models, Mon. Wea. Rev., 142, 3284–3302, 2014.

526   Chou, M., and Suarez, M.J.: An efficient thermal infrared radiation parameterization for use in

527   general circulation models, Technical Report Series on Global Modeling and Data

528   Assimilation, NASA Tech. Memo. 104606, 3, 85 pp, 1994.

529   Chow, F.K., and Street, R.L.: Evaluation of turbulence closure models for large-eddy simulation

530   over complex terrain: Flow over Askervein Hill, J. Appl. Meteor. Climatol., 48, 1050–1065,

531   2008.

532   Dudhia, J.: Numerical study of convection observed during the winter monsoon experiment

533   using a mesoscale two-dimensional model, J. Atmos. Sci., 46, 3077–3107, 1989.

534   Farr, T.G., Rosen, P.A., Caro, E., Crippen, R., Duren, R., Hensley, S., Kobrick, M., Paller, M.,

535   Rodriguez, E., Roth, L., Seal, D., Shaffer, S., Shimada, J., Umland, J., Werner, M., Oskin, M.,

536   Burbank, D., and Alsdorf, D.: The Shuttle Radar Topography Mission, Reviews of Geophysics,

537   45, RG2004, doi: 10.1029/2005RG000183, 2007.

538   Ferrier, B., Lin, Y., Parrish, D., Pondeca, M., Rogers, E., Manikin, G., Ek., M., Hart, M., DiMego,

539   G., Mitchell, K., Chuang, H.-Y.: Changes to the NCEP Meso Eta analysis and forecast system:

540   Modified cloud microphysics, assimilation of GOES cloud-top pressure, assimilation of

541   NEXRAD 88D radial wind velocity data, NWS Technical Procedures Bulletin, 2003.

542   Forthofer, J., Shannon, K., and Butler, B.: Simulating diurnally driven slope winds with

543   WindNinja, Eighth Symposium on Fire and Forest Meteorology. Oct 13-15. Kalispell, MT,

544   2009.

545   Forthofer, J.M., Butler, B.W., and Wagenbrenner, N.S.: A comparison of three approaches for

546   simulating fine-scale winds in support of wildland fire management: Part I. Model

547   formulation and accuracy, Int. J. Wildland Fire, 23, 969–981, 2014a.

548   Forthofer, J.M., Butler, B.W., McHugh, C.W., Finney, M.A., Bradshaw, L.S., Stratton, R.D,

549   Shannon, K.S., and Wagenbrenner, N.S.: A comparison of three approaches for simulating

550   fine-scale surface winds in support of wildland fire management. Part II. An exploratory

551   study of the effect of simulated winds on fire growth simulations, Int. J. Wildland Fire, 23,

552   982–994, 2014b.

553   Hong, S.-Y., Noh, Y., and Dudhia, J.: A new vertical diffusion package with an explicit treatment

554   of entrainment, Mon. Wea. Rev., 134, 2318–2341, 2006.

555   Janjic, Z.: Nonsingular implementation of the Mellor-Yamada level 2.5 scheme in the NCEP

556   meso model, NCEP Office Note No. 437, 60, 2002.

557   Kain, J.: The Kain-Fritsch convective parameterization: An update, J. Meteor. Climatol., 43, 170–

558   181, 2004.

559   Lacis, A.A., and Hansen, J.E., 1974: A parameterization for the absorption of solar radiation in

560   the earth's atmosphere, J. Atmos. Sci., 31, 118–133, 1974.

561   Lundquist, K.A., Chow, F.K., and Lundquist, J.K.: An immersed boundary method for the

562   Weather Research and Forecasting Model, Mon. Wea. Rev., 138, 796–817, 2010.

563   Mahrt, L.: Momentum balance of gravity flows, J. Atmos. Sci., 39, 2701–2711, 1982.

564   Mesinger, F., DiMego, G., Kalnay, E., Mitchell, K., Shafran, P.C., Ebisuzaki, W., Jovic, D., Woollen,

565   J., Rogers, E., Berbery, E.H., Ek, M.B., Fan, Y., Grumbine, R., Higgins, W., Li, H., Lin, Y.,

566   Manikin, G., Parrish, D., and Shi, W.: North American regional reanalysis, Bull. Amer.

567   Meteor. Soc., 87, 343–360, 2006.

568   Mlawer, E.J., Taubman, S.J., Brown, P.D., Iacono, M.J., and Clough, S.A.: Radiative transfer for

569   inhomogenous atmospheres: RRTM, a validated correlated-k model for the longwave, J.

570   Geophys. Res., 102, 16663–16682, 1997.

571   Scire, J.S., Robe, F.R., Fernau, M.E., and Yamartino, R.J.: A user's guide for the CALMET

572   meteorological model, Earth Tech, Inc., Concord. MA. Available online at

573   src.com/calpuff/download/CALMET_UsersGuide.pdf, 2000.

574   Scire, J.S., and Robe, F.R.: Fine-scale application of the CALMET meteorological model to a

575   complex terrain site, Air & Waste Management Associations's 90th Annual Meeting &

576   Exhibition, Toronto, Ontario, Canada, 16 pp, 1997.

577   Seaman, N.L., Gaudet, B.J., Stauffer, D.R., Mahrt, L., Richardson, S.J., Zielonka, J.R., and

578   Wyngaard, J.C.: Numerical prediction of submesoscale flow in the nocturnal stable

579   boundary layer over complex terrain, Month. Wea. Rev., 140, 956–977, 2012.

580   Skamarock, W.C., Klemp, J.B., Dudhia, J., Gill, D.O., Barker, D.M., Duda, M.G., Huang, X., Wang,

581   W., and Powers, J.G.: A description of the advanced research WRF version 3. NCAR Tech.

582   Note NCAR/TN-475STR, 2008.

583   Smirnova, T.G., Brown, J.M, and Benjamin, S.J.: Performance of different soil model

584   configurations in simulating ground surface temperature and surface fluxes, Mon. Wea.

585   Rev., 125, 1870–1884, 1997.

586   Smirnova, T.G, Brown, J.M., Benjamin, S.G., and Kim, D.: Parameterization of cold season

587   processes in the MAPS land-surface scheme, J. Geophys. Res., 105, 4077–4086, 2000.

588   Stauffer, D.R., and Seaman, N.L.: Multiscale four-dimensional data assimilation, J. Appl. Meteor.

589   33, 416–434, 1994.

590   Taylor, P.A., and Teunissen, H.W.: The Askervein Hill project: Overview and background data,

591   Bound.-Lay. Meteorol., 39, 15–39. 1987.

592   Thompson, G.R., Rasmussen, R.M., and Manning, K.: Explicit forecasts of winter precipitation

593   using an improved bulk microphysics scheme. Part I: description and sensitivity analysis,

594   Mon. Wea. Rev., 132, 519–542, 2004.

595

596   **Tables**

597   Table 1. Model specifications.

Model	Horizontal grid resolution	Number vertical layers	First layer height[a] (m AGL)	Top height[a] (m AGL)	Numerical core	Run frequency
NAM	12 km	26	200	15000	NMM	00z, 06z, 12z, 18z
WRF-UW	4 km	38	40	16000	ARW	00z, 12z
HRRR	3 km	51	8	16000	ARW	hourly
WRF-NARR	1.33 km	33	38	15000	ARW	NA
WindNinja	138 m	20	1.92	931	NA	NA

598   [a]Approximate average height AGL.

599

Table 2. Model mean bias, root-mean-square error (RMSE), and standard deviation of errors (SDE) for surface wind speeds and
directions during the 5-day evaluation period at Big Southern Butte. Downscaled values are in parentheses. Smaller values are in
bold. The 5-day period includes the Downslope, Upslope, and Externally-driven time periods.

Time period	Statistic	NAM	WRF-UW	HRRR	WRF-NARR
		Wind Speed (m s^{-1})			
5-day	Bias	-0.84 (**-0.67**)	-1.17 (**-0.95**)	-0.40 (**-0.14**)	-0.31 (**-0.08**)
	RMSE	2.31 (**2.04**)	2.39 (**2.07**)	2.52 (**2.47**)	2.33(**2.21**)
	SDE	2.15 (**1.92**)	2.08 (**1.83**)	2.49 (**2.47**)	2.31 (**2.21**)
Downslope	Bias	-1.07 (**-0.76**)	-1.15 (**-0.74**)	**-0.09** (0.48)	-0.48 (**0.12**)
	RMSE	2.08 (**1.92**)	2.03 (**1.83**)	**2.36** (2.66)	**2.19** (2.28)
	SDE	1.79 (**1.77**)	**1.67** (1.68)	**2.36** (2.62)	**2.14** (2.28)
Upslope	Bias	-0.81 (**-0.74**)	-1.11 (**-0.98**)	-0.81 (**-0.75**)	0.06 (**0.05**)
	RMSE	1.73 (**1.62**)	2.02 (**1.86**)	1.93 (**1.81**)	1.86 (1.86)
	SDE	1.52 (**1.44**)	1.69 (**1.58**)	1.76 (**1.64**)	1.86 (1.86)
Externally-driven	Bias	**-0.57** (-0.62)	**-1.28** (-1.32)	**-0.94** (-1.03)	**-0.22** (-0.33)
	RMSE	3.06 (**2.48**)	3.21 (**2.58**)	3.17 (**2.59**)	2.92 (**2.39**)
	SDE	3.00 (**2.40**)	2.94 (**2.22**)	3.02 (**2.38**)	2.92 (**2.37**)
		Wind Direction (°)			
5-day	Bias	59 (**56**)	57 (**53**)	64 (**60**)	57 (**54**)
	RMSE	76 (**72**)	74 (**71**)	80 (**76**)	73 (**71**)
	SDE	47 (**46**)	47 (**46**)	47 (**46**)	46 (46)
Downslope	Bias	67 (**60**)	61 (**56**)	76 (**67**)	66 (**61**)
	RMSE	83 (**77**)	78 (**72**)	88 (**81**)	81 (**75**)
	SDE	49 (**47**)	48 (**46**)	46 (46)	47 (**45**)
Upslope	Bias	55 (**52**)	58 (**54**)	56 (56)	52 (**49**)
	RMSE	70 (**67**)	74 (**71**)	72 (72)	68 (**65**)
	SDE	44 (**42**)	46 (**45**)	45 (46)	44 (**42**)
Externally-driven	Bias	**48** (49)	**45** (46)	51 (**50**)	44 (**46**)
	RMSE	**64** (65)	**63** (65)	68 (**67**)	**62** (65)
	SDE	**43** (44)	**44** (47)	45 (**44**)	**43** (46)

604   **Figures**
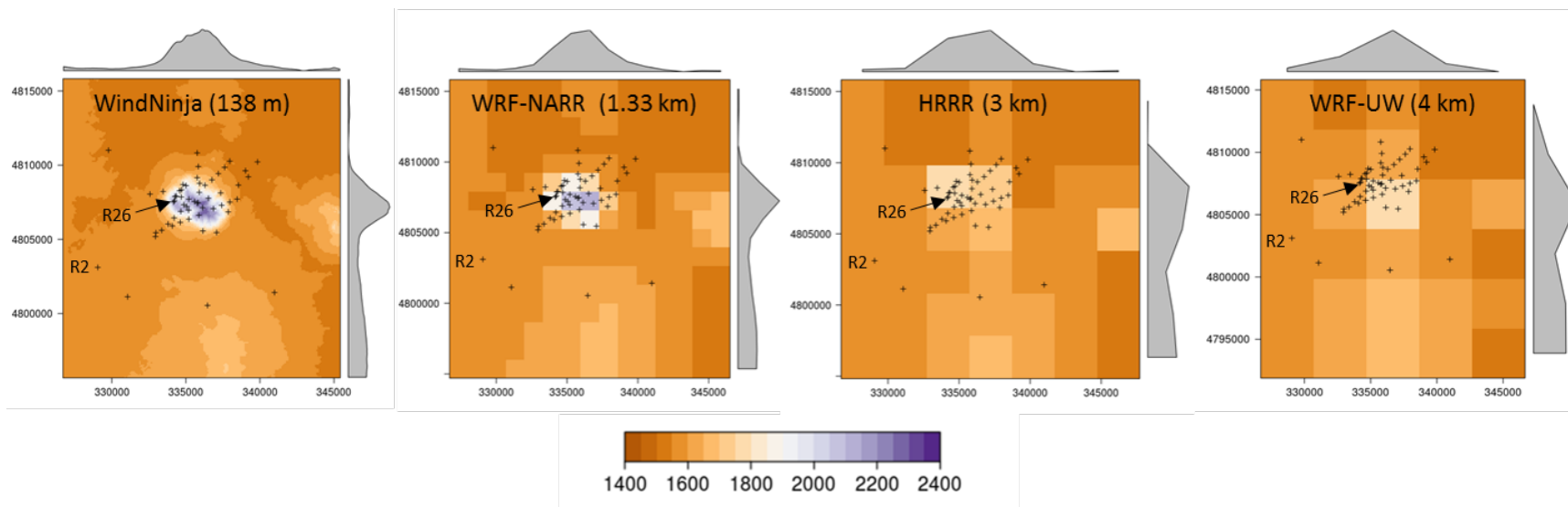

605
606
607   Figure 1. Terrain representation (m ASL) in WindNinja, WRF-NARR, HRRR, and WRF-UW for the Big Southern Butte. Crosses indicate

608   surface sensor locations. Maps are projected in the Universal Transverse Mercator (UTM) zone 12 coordinate system. Axis labels are

609   eastings and northings in m. Profiles in gray are the average elevations for rows and columns in the panel. NAM (12 km) terrain is

610   represented by just four cells and is not shown here.

611

612
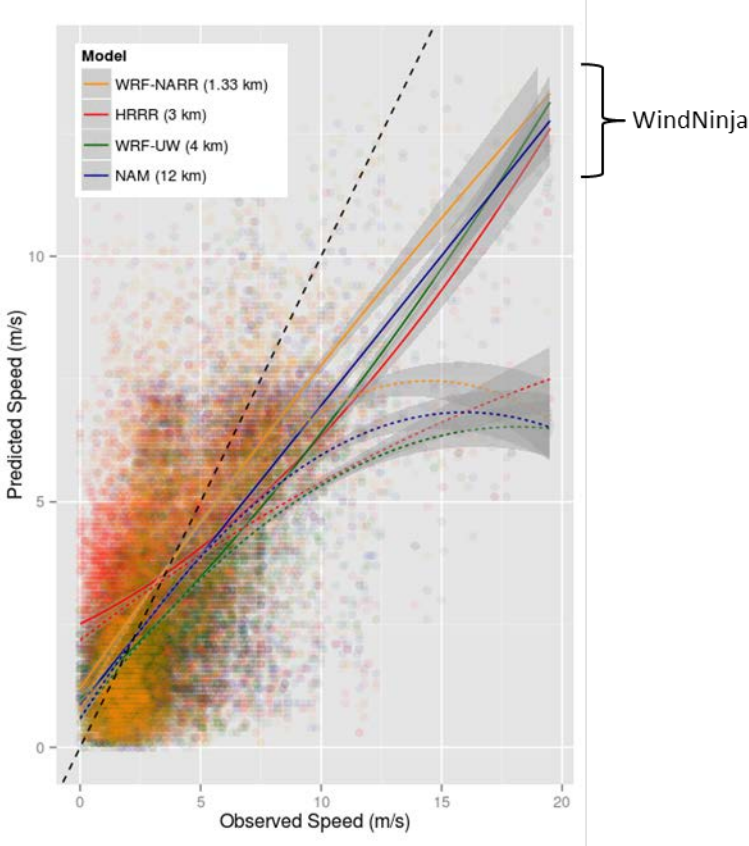
Figure 2. Observed vs. predicted wind speeds for the 5-day evaluation period at Big Southern

Butte. Dashed black line is the line of agreement. Colored lines are linear regressions

(quadratic fit); dashed lines are NWP models and solid lines are NWP forecasts downscaled with

WindNinja. Shading indicates 95% confidence intervals.

617
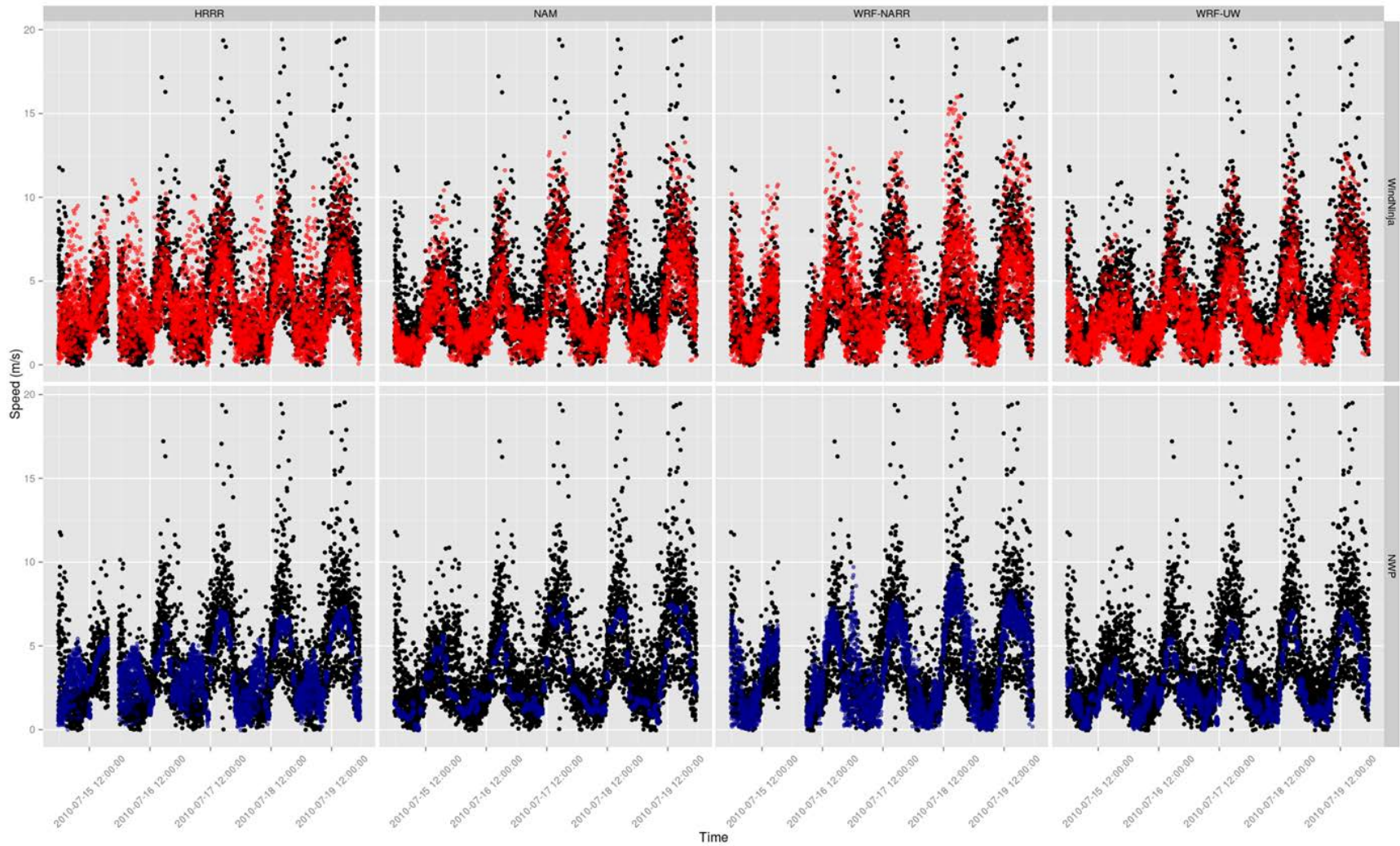
618
619   Figure 3. Observed (black) and predicted (colored) winds speeds at all sensors for 15 July 2010–19 July 2010 at Big Southern Butte.

620   Top panels are WindNinja predictions. Bottom panels are NWP predictions.
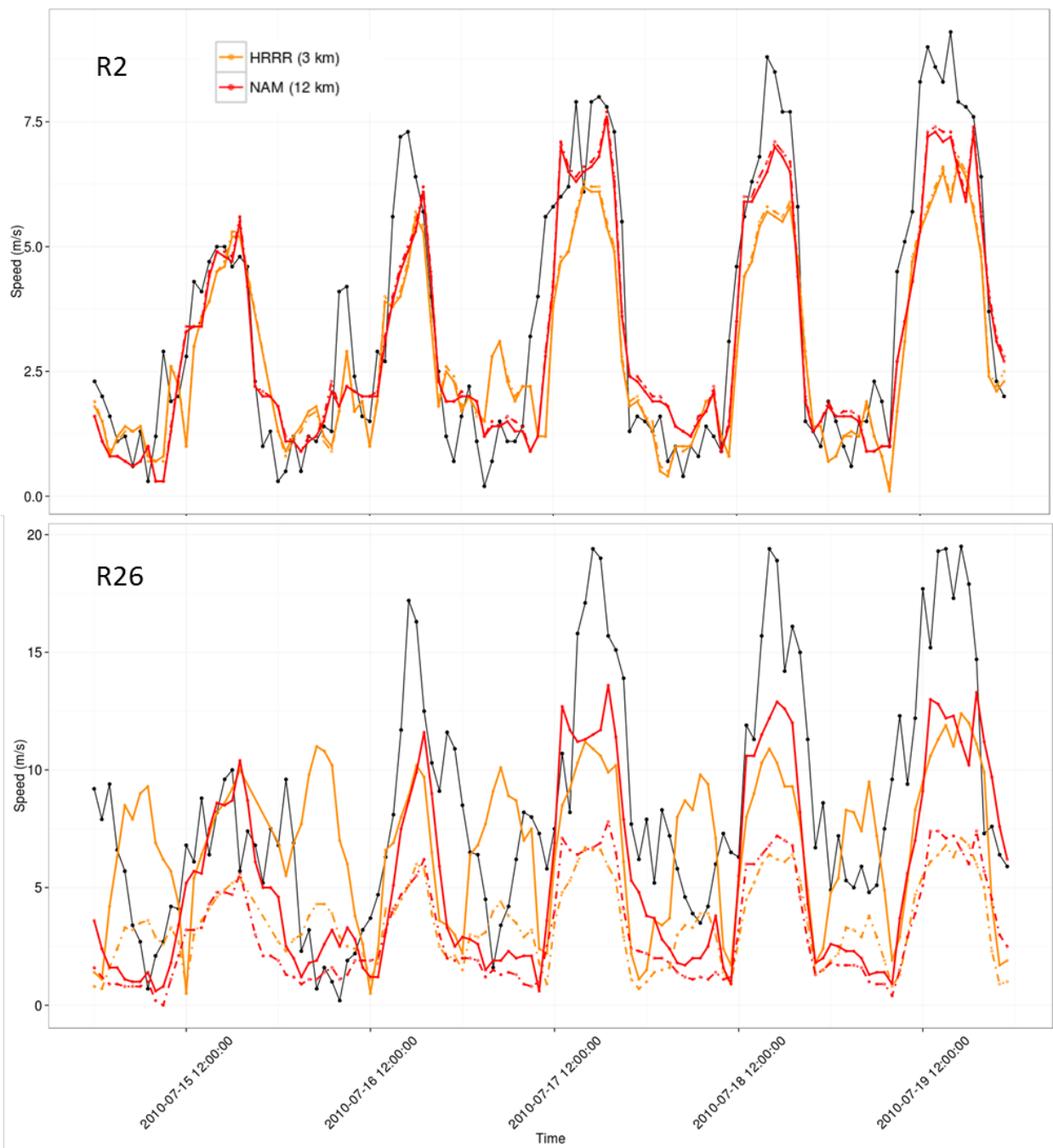
621

622   Figure 4. Observed (black line) and predicted (colored lines) wind speeds for sensor R2 located

623   5 km southwest of Big Southern Butte on the Snake River Plain and sensor R26 located on a

624   ridgetop. Dashed colored lines are NWP models and solid colored lines are WindNinja.
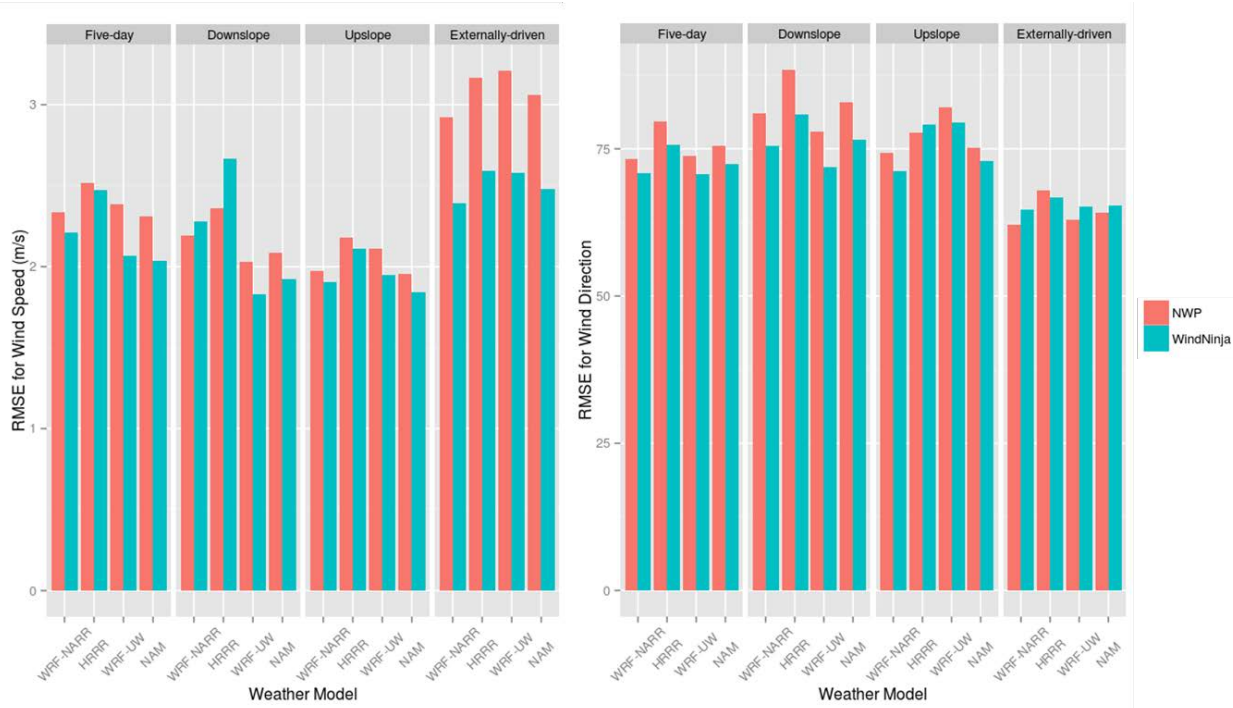
Figure 5. Root-mean-square error in wind speed (left) and wind direction (right) at Big Southern Butte for the five-day evaluation period (N = 4149), and downslope (N = 1593), upslope (N = 717), and externally -driven (N = 966) periods within the five-day period. Sample size, N = number of hours x number of sensor locations.

630
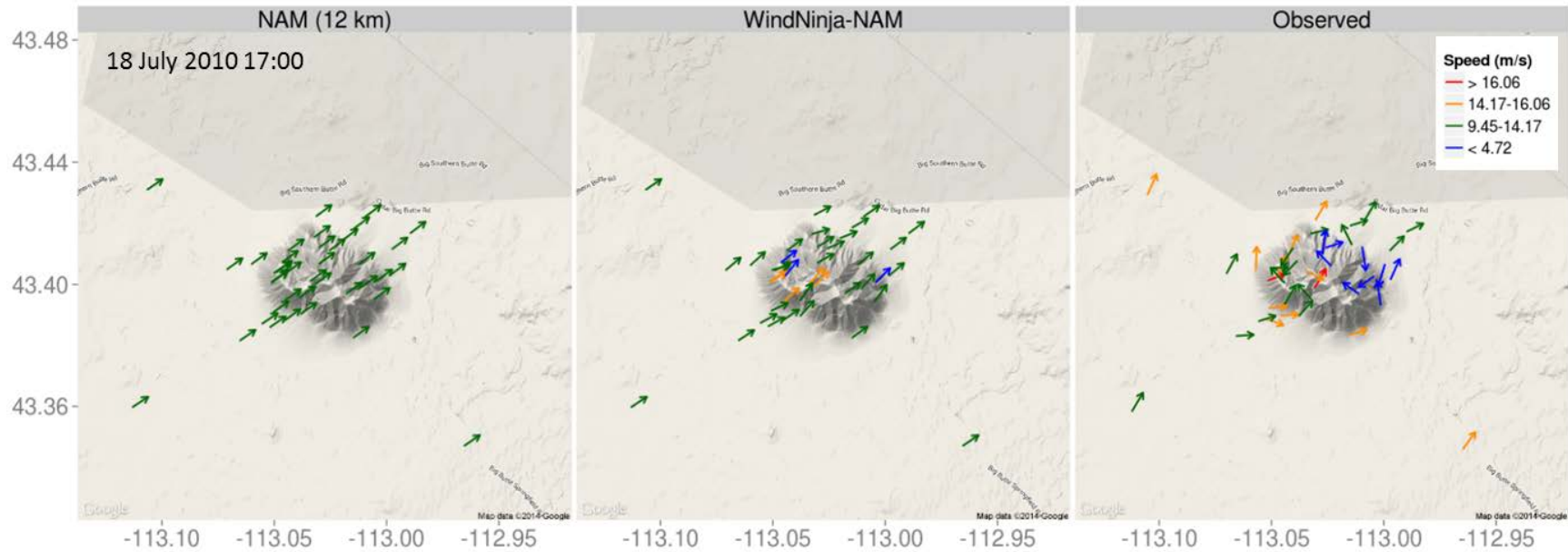
Figure 6. Predicted and observed winds for an externally-forced flow event at Big Southern Butte.

632

633
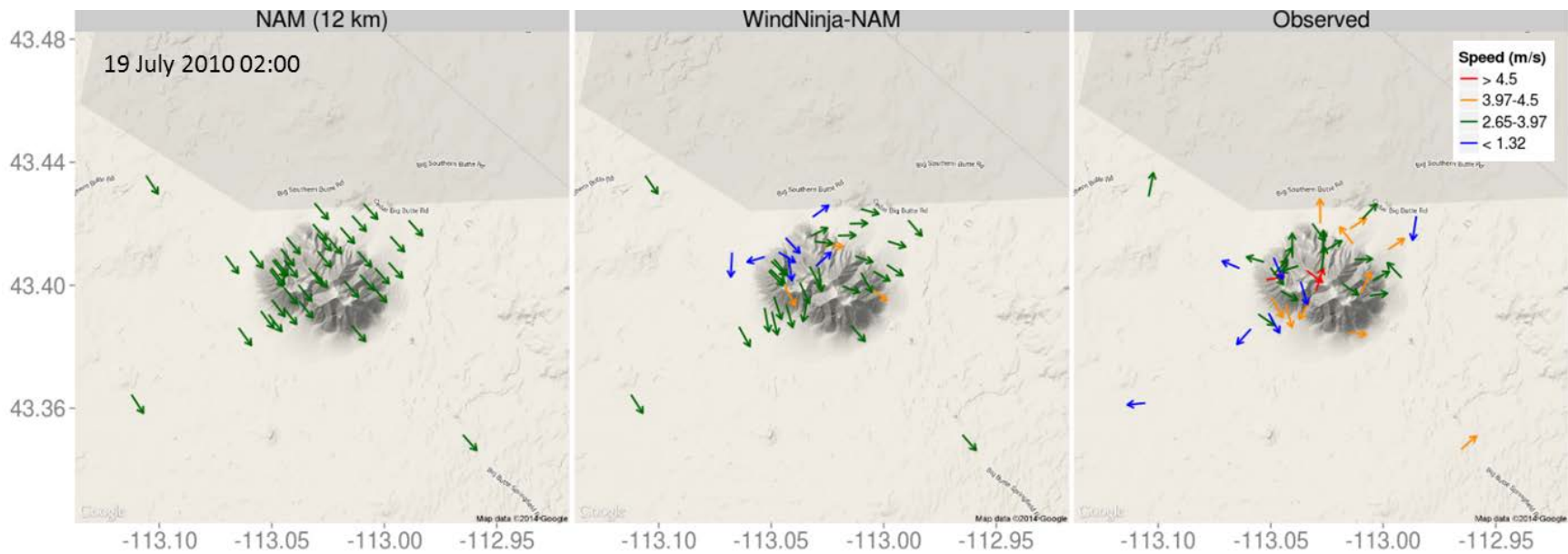
Figure 7. Predicted and observed winds for a downslope flow event at Big Southern Butte.

635
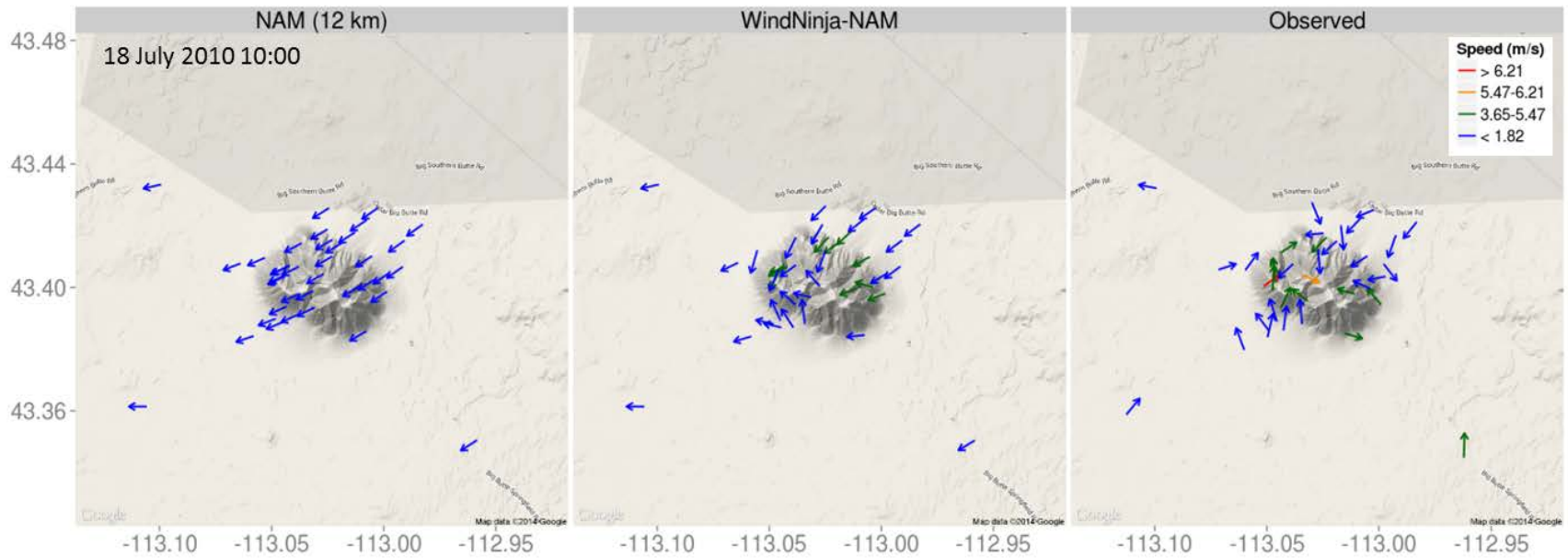
636

637   Figure 8. Predicted and observed winds for an upslope flow event at Big Southern Butte.

638